CHEMISTRY
A EUROPEAN JOURNAL

DOI: 10.1002/chem.200801234

Bi_2O_3 Hierarchical Nanostructures: Controllable Synthesis, Growth Mechanism, and their Application in Photocatalysis

Lin Zhou, Wenzhong Wang,* Haolan Xu, Songmei Sun, and Meng Shang[a]

Abstract: By introducing VO_3^- into the reaction system, uniform hierarchical nanostructures of Bi_2O_3 have been successfully synthesized by a template-free aqueous method at 60–80 °C for 6 h. The as-prepared hierarchitectures are composed of 2D nanosheets, which intercross with each other. Based on the electron microscope observations, the growth of such hierarchitectures has been proposed as an Ostwald ripening process followed by self-assembly. The nucleation, growth, and self-assembly of Bi_2O_3 nanosheets could be readily tuned, which brought different morphologies and microstructures to the final products. Pore-size distribution analysis revealed that both mesopores and macropores existed in the product. UV-vis spectroscopy was employed to estimate the band gap energies of the hierarchical nanostructures. The photocatalytic activities of as-prepared Bi_2O_3 hierarchitectures were 6–10 times higher than that of the commercial sample, which was evaluated by the degradation of RhB dye under visible light irradiation ($\lambda > 420$ nm).

Keywords: bismuth oxide · crystal growth · nanostructures · photochemistry

Introduction

In recent years, considerable interest has been focused on the synthesis of inorganic nanomaterials with controllable morphology, orientation, dimensionality etc., which usually exhibit unique properties. This makes it possible for the design of new functional nanomaterials.[1] In particular, the self-assembly of low dimensional (0D, 1D, 2D) nanostructures into three-dimensional (3D) superstructures represents a hot topic, owing to their potential applications in electronic, magnetic, optoelectronic, catalytic, and biomedical fields.[2] A number of inorganic materials with hierarchical superstructures, including metal, metal oxide, hydrate, sulfide, etc., have been fabricated. Nonetheless, oriented assembly of nanorods, nanotubes, and nanoplates etc. is generally difficult. It usually requires hard or soft templates to control their oriented growth,[3] which not only introduces heterogeneous impurities, but also increases production costs. Therefore, the development of facile, template-free, and self-assembly routes for the formation of hierarchical nanostructures is of great interest. Moreover, although much effort has been made, the rational design of 3D nanomaterials with ideal and controllable morphologies, sizes, and structures still remains a challenge.

Bismuth oxide (Bi_2O_3) has been widely used in gas sensors, solid oxide fuel cells, optical coatings, ceramic glass manufacturing etc., owing to their excellent properties, such as high refractive index, high dielectric permittivity, as well as marked photoluminescence properties.[4–9] Furthermore, Bi_2O_3 has also proved to be a good photocatalyst for water splitting and pollutant decomposing under visible light irradiation. Recently, Bi_2O_3 nanocrystals with various morphologies have been achieved. For example, ultrathin Bi_2O_3 nanowires have been prepared by using an oxidative metal vapor transport deposition technique.[10] Bi_2O_3 sub-micrometer rods have been produced using BiI_3 and O_2 as a starting material.[11] Yu et al.[12] fabricated Bi_2O_3 nanoplates directly from commercial bulk bismuth oxide crystals by hydrothermal treatment. Very recently, Li et al.[13] reported the synthesis of Bi_2O_3 nanotubes from oxidizing the bismuth nanowires in air by a templates-based heat-treatment method. As the photocatalytic activity closely interrelates with the size, morphology, and microstructures of the photocatalysts, the availability of Bi_2O_3 hierarchical nanostructures with well-defined morphologies and dimensions should enhance their photocatalytic property and is, therefore, highly desirable

---

[a] L. Zhou, Prof. W. Wang, H. Xu, S. Sun, M. Shang
State Key Laboratory of High Performance Ceramics
and Superfine Microstructures
Shanghai Institute of Ceramics, Chinese Academy of Sciences
1295 Dingxi Road Shanghai 200050 (P. R. China)
Fax: (+86) 21-5241-3122
E-mail: wzwang@mail.sic.ac.cn

Supporting information for this article is available on the WWW under http://dx.doi.org/10.1002/chem.200801234.

from the practical point of view. However, to the best of our knowledge, there is no report on a controllable assembly of bismuth oxide nanoplates into 3D superstructures.

Herein, for the first time we report the morphology and assembly-controlled synthesis of Bi_2O_3 3D nanostructures through a facile template-free approach, The addition of VO_3^- mediated the nucleation and growth of Bi_2O_3, leading to the in-situ self-assembly of 3D hierarchitectures from 2D nanosheets. The organization of Bi_2O_3 nanosheets can be tailored to obtain the superstructures with different shapes by varying the amount of VO_3^- and reaction temperature. The morphology evolution and the growth mechanism were investigated carefully, based on the electron microscopy observation. In addition, the Bi_2O_3 hierarchitectures product exhibited 6–10 times higher photocatalytic activity over commercial sample under visible light irradiation.

Results and Discussion

Structure and Morphology: The phase and composition of the products were characterized by X-ray diffraction (XRD). Figure 1 shows the XRD pattern of the sample obtained by a mild aqueous route at 60 °C when the VO_3^- concentration was 2 mmol L^{-1}. All the diffraction peaks can be indexed to a cubic phase of δ-Bi_2O_3 (JCPDS card No.27–0052, $a = 5.525$ Å). No other crystalline impurities were detected, demonstrating the phase purity of the Bi_2O_3 products. The broadening of the peaks indicates that the crystallites are small. Bismuth oxide has four main crystalline phases: monoclinic α, tetragonal β, body centered cubic γ, and face-centered cubic δ.[13–15] Among these phases, the δ-phase is the high-temperature phase, which usually exists at above 730 °C. In the present case, the cubic δ-Bi_2O_3 have been successfully synthesized at very low temperature.

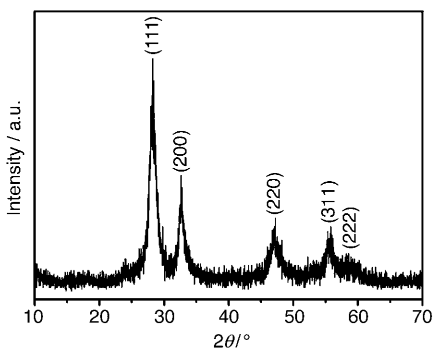

Figure 1. XRD patterns of the products obtained by a mild aqueous route at 60 °C, $VO_3^- = 2$ mmol L^{-1}.

The morphology of the final products was characterized by SEM and TEM. Figure 2a is a typical low-magnification SEM image of the as-synthesized product obtained at 60 °C, which clearly reveals that the sample consists of uniform spheres with an average diameter of ≈6 μm. The magnified image in Figure 2b shows that the spheres are flower-like and exhibit an hierarchical structure. To reveal the detailed structure of the flowers, high magnification SEM images were recorded. Figure 2c,d clearly demonstrate the surface structure of the flower, from which one can see that dozens of 2D sheets (with a side length of 1–2 μm and a thickness of about 30 nm) are intercrossed with each other and have formed flowery microspheres through self-assembly. Although these sheets are not highly close-packed, all of the microflowers maintained their integrity after vigorous ultrasonic treatment, showing the structural stability of the product.

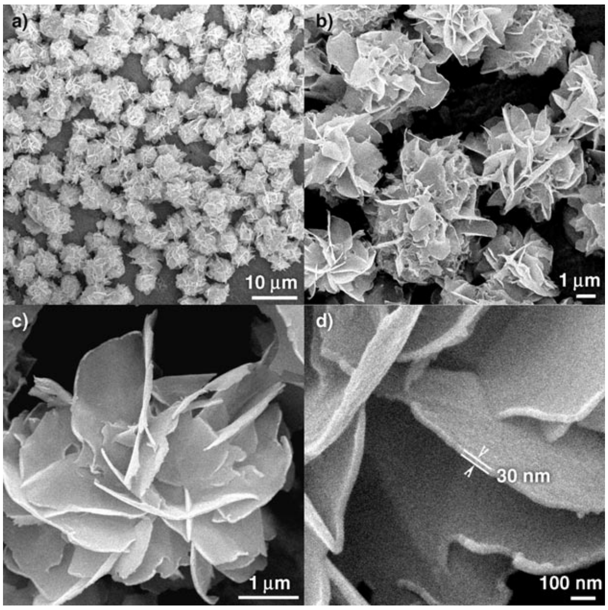

Figure 2. SEM images of the Bi_2O_3 samples prepared at 60 °C, $VO_3^- =$ 2 mmol L^{-1}: a) Overall product morphology; b) Enlarged SEM image of the spheres, showing flower-like morphology; c) Detailed view of an individual sphere; d) Magnified image of the surface structure of the sphere.

TEM images (Figure 3a,b) of the sample further confirmed the loose-packed flowery structure of the microspheres. Figure 3c shows an enlarged TEM image of a single sheet marked by a circle. The corresponding selected area electron diffraction (SAED) pattern (inset in Figure 3c) with a regular and clear square diffraction spot array reveals that each petal is single crystalline. The high resolution TEM (HRTEM) image (Figure 3d) is recorded on the corner of the sheet. The clear lattice fringe indicates the single crystalline nature of the plates. The interplanar spacings are 0.276 nm and 0.274 nm, which correspond to the (200) and (020) planes of cubic Bi_2O_3, respectively. Both the HRTEM and SAED analyses indicate the anisotropic growth of the plates along (200) and (020) directions.

The as-synthesized product obtained at 80 °C displays a different flowery morphology with an average diameter of 8–10 μm, as shown in Figure 4a. Closer observation (Figure 4b,c) demonstrates that the flowers are composed of smaller nanosheets with the side length of ≈500 nm and the thickness of ≈40 nm. Comparing with the ones obtained at

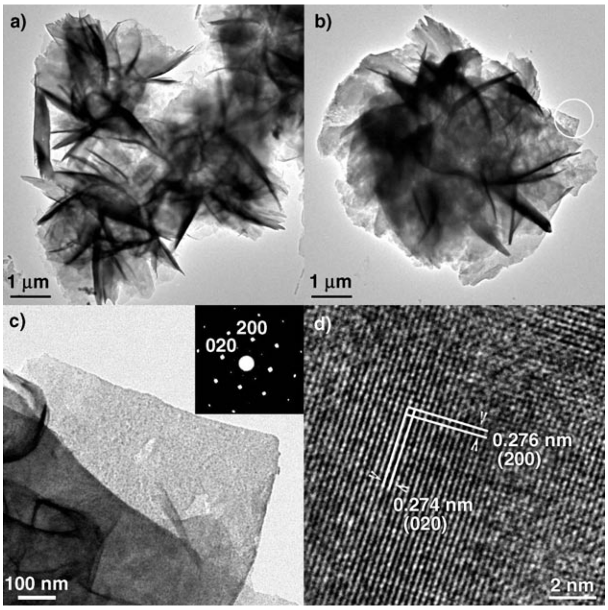

Figure 3. a) Low-magnification TEM image of the Bi_2O_3 hierarchitectures; b) High-magnification TEM image of an individual flower; c) TEM image of a single nanosheet taken from the circle of b). Inset: the corresponding SAED pattern of the nanosheet; d) HRTEM images of the nanosheet recorded on the corner of a sheet.

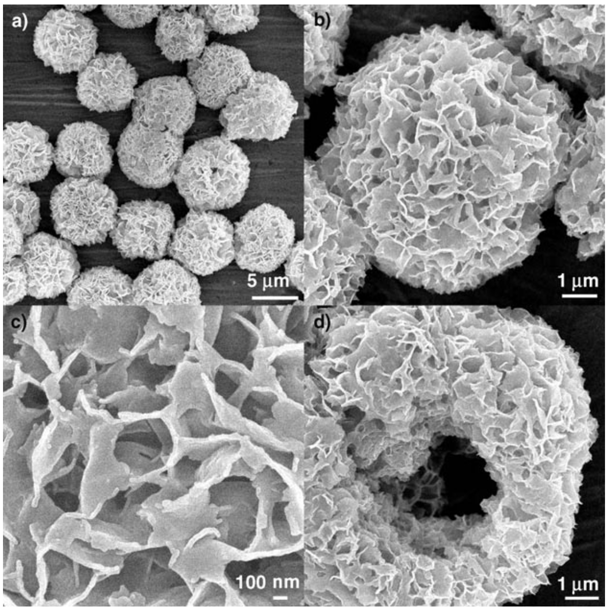

Figure 4. SEM and TEM images of the Bi_2O_3 samples prepared at 80 °C, VO_3^- = 2 mmol L^{-1}: a) Overall product morphology; b) Detailed view of an individual sphere; c) Magnified SEM image of the surface structure of the sphere; d) An incomplete or cracked microsphere morphology.

60 °C, when the VO_3^- concentration was 2 mmol L^{-1}, these nanosheets are densely-packed, exhibiting a porous structure with an aperture of 500–800 nm. The porous structure was revealed by the magnified SEM image (Figure 4d), which shows an incomplete or cracked microsphere in which the inner structure can be clearly seen. Despite the morphology difference, the XRD pattern of the sample presents similar profile to that prepared at 60 °C.

Growth mechanism: To investigate the growth mechanism of the Bi_2O_3 hierarchical structure, the growth processes were systematically studied by analyzing the samples at different growth stage. Figure 5a–f show a series of SEM images of the precursor and products by varying the reaction time from 2 h to 4 h, 6 h, 12 h, and 24 h at 60 °C, when the VO_3^- concentration was kept at 2 mmol L^{-1}. As shown in Figure 5a, the precursor is composed of irregular nanoparticles with size of ≈100 nm. After 2 h of reaction, some dense aggregates with a diameter of 2–5 µm can be found (Figure 5b). These aggregates became looser when the reaction time was longer (4 h, Figure 5c). The product obtained after 6 h contains a mixture of flower structures, particle aggregates, and dispersed nanoparticles (Figure 5d). The flowery structures are constructed by lots of small nanosheets (0.5–1 µm in width) intercrossed with each other. Prolonging the reaction time to 12 h gave microflowers as the dominant product (Figure 5e), only a small amount of nanoparticles remained (≈5 %). For a reaction time of 24 h, well-defined microflowers were formed, which consisted of nanosheets (1–2 µm in width, Figure 5f).

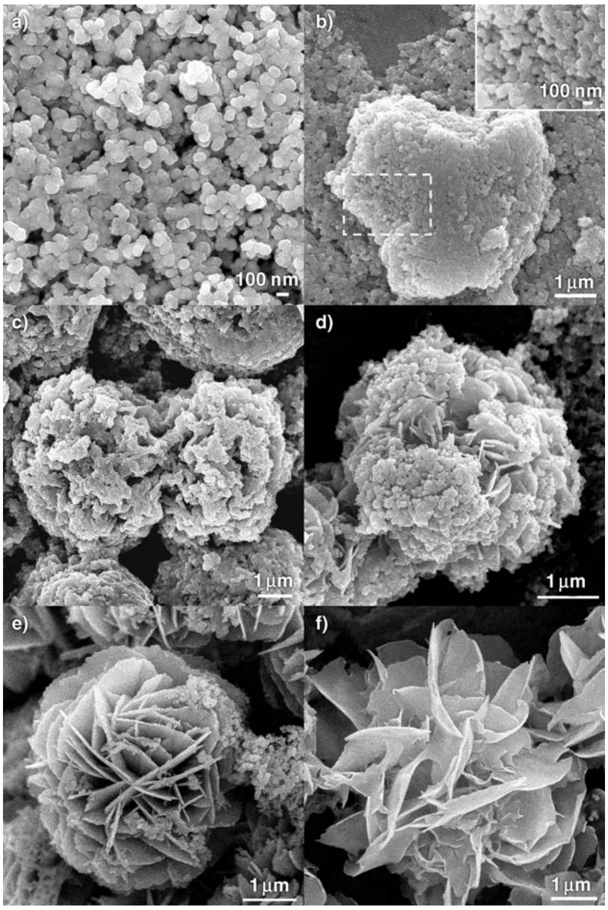

Figure 5. SEM images of a) the precursor and the Bi_2O_3 products obtained at various reaction stages b) 2 h, c) 4 h, d) 6 h, e) 12 h and f) 24 h.

On the basis of above experimental results, we considered that the formation of the novel flowery hierarchical structure was a cooperation effect of Ostwald ripening and self-assembly process. The whole process is illustrated in Figure 6. In the first stage, tiny crystalline nuclei were generated in the supersaturated solution and grew into nanoparticles. As no surfactants or templates were involved, these nanoparticles were quickly built and spontaneously aggregated into large spheres to minimize their surface area through the process known as Ostwald ripening.[16] The numerous small protuberances on the surface of the microspheres could provide many high-energy sites for nanocrystals grow.[17] Under constant reaction at 80 °C, the microspheres started to dissolve into the solution and spontaneously nucleate onto these protuberances. Then the crystallized particles grew aniscopically along the 2D direction, resulting in the formation of the nanosheets. As the mass diffusion and Ostwald ripening process proceeded, the nanosheets grew until all the nanoparticles were consumed, accompanied by their self-organization into the flowery structure. The different morphology of the two products can be ascribed to the effect of nucleation-dissolution-recrystallization rate. At a relatively higher temperature, 80 °C, the solubility of precursor is increased. The increase of the solubility of precursor will result in the increase of reactant (Bi^{3+} and OH^-) concentrations in solution. So the nucleation and growth rate were increased. With the reactants transferred onto the surface of the microspheres, numerous nanosheets grew and intercrossed, which restrains the expanding of each nanosheet.

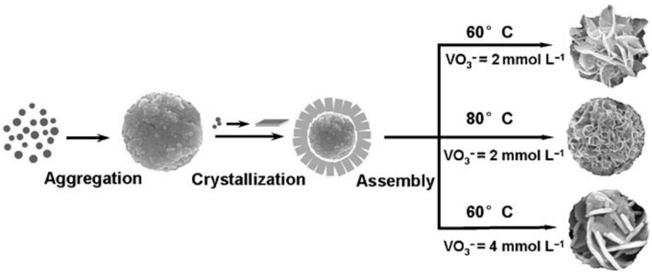

Figure 6. Schematic illustration of the proposed formation mechanism of Bi_2O_3 hierarchical nanostructures.

Influences of reaction conditions: It is noticeable that the existence of VO_3^- was crucial in the formation of the nanosheets and their self-assembly. The flower-like products could only be obtained in the presence of appropriate amount of VO_3^-. Other agents, such as WO_6^-, MoO_4^- instead of VO_3^-, have been applied in the reaction system. No flowery structures or uniform products could be observed. Therefore, the effect of VO_3^- on the product was investigated. Controlled experiments were conducted in the presence of different amounts of VO_3^- at 60 °C, but the reaction time, and reactant concentration were the same as those in the typical synthesis. If no VO_3^- was introduced in the reaction system, only irregular particles with various shapes can be observed. Corresponding XRD measurements indicated that the product is poorly crystallized (Figure S1a in the Supporting Information). When the VO_3^- concentration was increased to 0.25 mmol L^{-1}, a mixture of spherical nanoparticles (≈150 nm in diameter) and 3D flower-like superstructures formed, as shown in Figure 7a–c. A pure cubic phase of Bi_2O_3 can be identified from the corresponding XRD pattern, no peaks of impurities were detected (Figure S1b in the Supporting Information). More than 0.5 mmol L^{-1} VO_3^- is necessary to obtain the pure flower-like structures that consist of nanosheets. This is to say the formation of the nanosheets and their assembly are attributed to the presence of VO_3^- in the present system. Further increasing the concentration of VO_3^- in the reaction system gave another type of 3D hierarchical structure. Figure 8a is the overall view of the sample prepared at 60 °C, 4 mmol L^{-1} VO_3^-, showing that the product contains lots of microspheres with a diameter of ≈1 μm. The magnified SEM image (Figure 8b) shows that the surfaces of these spherical structures are also constructed by many nanosheets and take on a flower-like appearance. Compared with the sample shown in Figure 2, the average diameter of the microflowers is smaller and the nanopetals are more loosely packed. Closer observation of a typical flower-like structure, as shown in Figure 8c,d, reveals that the nanosheets are smaller (300–500 nm in size) but thicker (≈50 nm). This experimental phenomena can be rationally explained as a concentration effect of reactant (Bi^{3+} and OH^-) resulting from the interaction of VO_3- ions with Bi^{3+} in the solution. The probable reaction processes in aqueous solution can be summarized in Equations (a)–(c):

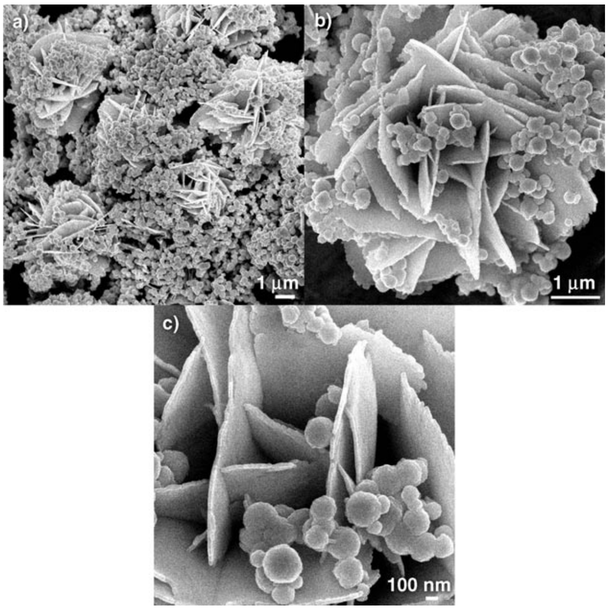

Figure 7. SEM images of the Bi_2O_3 product prepared at 60 °C, VO_3^- = 0.25 mmol L^{-1}.

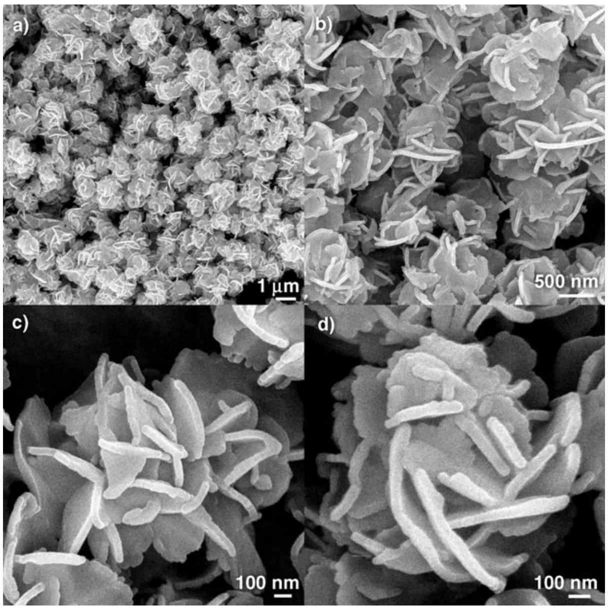

Figure 8. a) Low-magnification SEM image and b) High-magnification SEM image of the Bi_2O_3 product prepared at 60 °C, $VO_3^- = 4\ mmol\,L^{-1}$; c–d) Detailed view of an individual sphere.

$$Bi^{3+} + H_2O + NO_3^- \rightarrow BiONO_3 \downarrow + 2\,H^+ \qquad (a)$$

$$2\,BiONO_3 + 2OH^- \rightarrow Bi_2O_3 \downarrow + 2\,NO_3^- + H_2O \qquad (b)$$

$$BiONO_3 + VO_3^- \rightarrow BiVO_4 \downarrow + NO_3^- \qquad (c)$$

$Bi(NO_3)_3$ was first strongly hydrolyzed in water to produce slightly soluble $BiONO_3$ [Eqn. (a)].[18] If no VO_3^- is added in the solution, Bi_2O_3 will appear immediately, owing to the fast reaction rate of $BiONO_3$ and OH^- under the present reaction condition, as showing in Equation (b). However, with the addition of VO_3^- into the reaction system, $BiVO_4$ will generate firstly in the form of amorphous at relatively low pH value [Eqn. (c)], as reported in our previous work.[19] Under constant heat treatment on the aqueous solution, the amorphous product gradually dissolved. When the pH value was increased, the existence of large quantities of OH^- forces the Equation (b) shift towards the right side and speeds up the dissolution of the amorphous $BiVO_4$ to release $BiONO_3$. It is reasonable that the Equation (b) and the Equation (c) compete with each other and thus moderates the nuclearation and growth rate of Bi_2O_3, which results in the formation of the flower-like superstructures. Moreover, we found that only by increasing the pH value to 12, could the formation of Bi_2O_3 crystals and their subsequent self-assembly be realized. However, the higher pH value (> 13) does not favor the formation of microflower but nanoparticles with a size of ≈100 nm (Figure S2 in the Supporting Information). These results indicate that the morphologies of the products are strongly pH-dependent, which can be also confirmed by the above reaction equations.

Nitrogen sorption: The nitrogen adsorption-desorption isotherms and porosity of the different samples are presented in Figure 9. According to BDDT classification, all the samples display a type IV isotherm with a type H3 hysteresis loop (at $P/P_0 > 0.8$), implying the presence of mesopores (2–50 nm in size).[20] Moreover, it can be seen that the hysteresis loop shifts approach $P/P_0 = 1$, indicating the existence of macropores (> 50 nm).[20] These results were further confirmed by the corresponding pore-size distributions in which the peaks for both mesopores and macropores up to 100 nm can be found, as shown in the insets of Figure 9. Considering

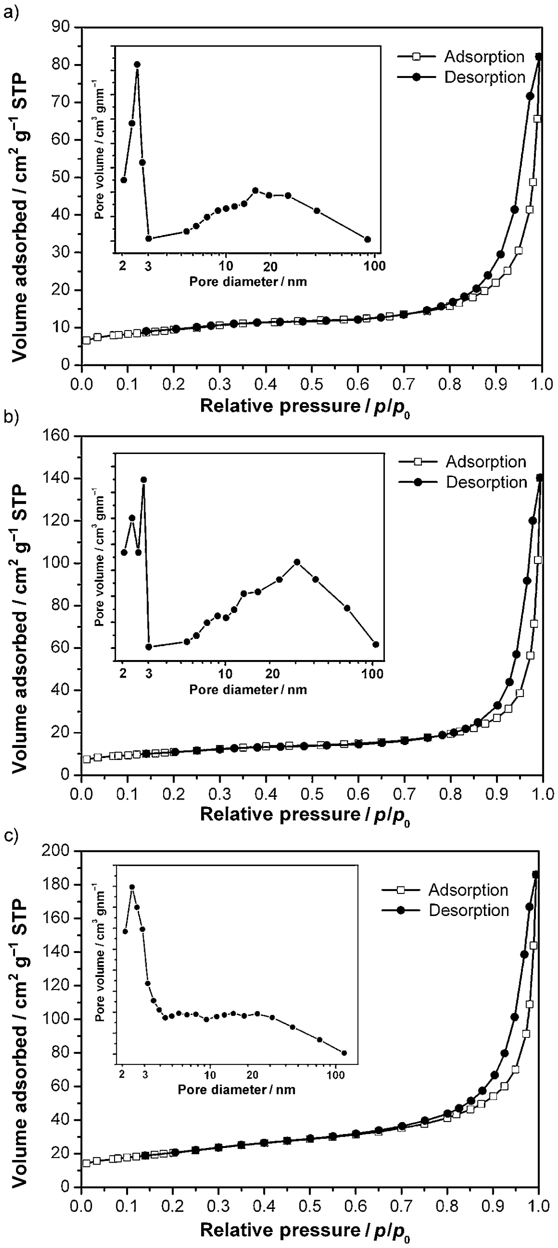

Figure 9. Typical N_2 gas adsorption-desorption isotherm of the Bi_2O_3 products a) at 60 °C, $VO_3^- = 2\ mmol\,L^{-1}$; b) at 60 °C, $VO_3^- = 4\ mmol\,L^{-1}$; c) at 80 °C, $VO_3^- = 2\ mmol\,L^{-1}$. Inset: the corresponding pore-size distribution.

the observed morphology of the product, the smaller pores with a sharp peak at about 2.5 nm may be generated during the crystal growth process, whereas the larger pores with a wide pore size distribution can be attributed to the space between the intercrossed Bi_2O_3 nanosheets.[21] The Brunauer–Emmett–Teller (BET) surface area, pore volumes, and mean pore diameters of the as-prepared samples are summarized in Table 1.

Table 1. The Brunauer–Emmett–Teller (BET) surface area, pore volumes, and mean pore diameters of the as-prepared samples.

Sample	Reaction conditions		BET surf. areas	Pore volumes	Mean pore diameters
	T [°C]	$C_{VO_3^-}$ [mmol L^{-1}]	[m^2 g^{-1}]	[cm^3 g^{-1}]	[nm]
a	60	2	33.1	0.12	20.6
b	60	4	38.6	0.22	27.3
c	80	2	72.9	0.29	16.1

Optical properties and photocatalytic activity: The optical properties of the Bi_2O_3 samples were measured by using UV-vis spectroscopy. Figure 10 shows the diffuse reflectance spectra of the different Bi_2O_3 samples. The steep absorption edge in the visible range confirms that the band gap is owed to the intrinsic transition of the nanomaterials but not a result of the transition from impurity level.[22] It is known that the optical absorption coefficient near the band edge follows the equation $(\alpha h\nu)^2 = A(h\nu - E_g)$ for a direct-bandgap material in which α, h, ν, E_g, and A are the absorption coefficient, Planck constant, light frequency, band gap, and a constant, respectively.[23] This relationship gives the band gap (E_g) by extrapolating the straight portion of $(\alpha h\nu)^2$ against $h\nu$ plot to the point $\alpha = 0$, which are 2.93 eV, 3.02 eV and 3.10 eV for the samples prepared at 60 °C, $VO_3^- =$ 2 mmol L^{-1}; at 60 °C, $VO_3^- =$ 4 mmol L^{-1} and at 80 °C, $VO_3^- =$ 2 mmol L^{-1}, respectively. These values were a little bigger than the reported value (2.85 eV), which could be associated with the nanosized effect.[24]

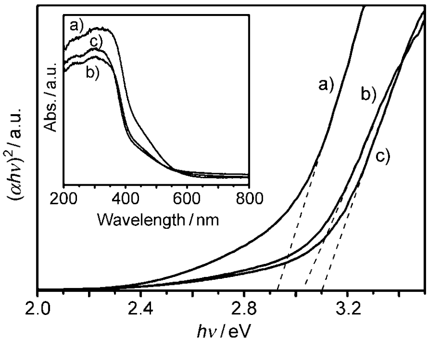

Figure 10. UV-vis diffuse reflectance spectra of the Bi_2O_3 products obtained a) at 60 °C, $VO_3^- =$ 2 mmol L^{-1}; b) at 60 °C, $VO_3^- =$ 4 mmol L^{-1}; c) at 80 °C, $VO_3^- =$ 2 mmol L^{-1}, respectively.

Photocatalytic activities of the Bi_2O_3 hierarchitectures were evaluated by the degradation of RhB dye in water under visible light irradiation ($\lambda > 420$ nm). The characteristic absorption of RHB at $\lambda = 553$ nm was used to monitor the photocatalytic degradation process. The temporal evolution of the spectral changes taking place during the photodegradation of RhB over as-prepared samples is displayed in Figure 11. A control experiment showed that in the absence of Bi_2O_3 powders the absorption intensity of the RhB hardly changed with increasing irradiation time, which demonstrated that the as-prepared Bi_2O_3 hierarchitectures are active photocatalysts. For comparison, the same photodegradation experiment using commercial Bi_2O_3 (Shanghai Chemical Company) was also carried out. It is clear that the photodegradation rates of the as-synthesized Bi_2O_3 hierarchitectures are much higher (6–10 times) than that of the corresponding commercial sample. Among them, the sample prepared at 80 °C exhibited the highest photocatalytic activity, indicating that the increase of the BET surface areas (from 33.06 m^2 g^{-1} to 72.87 m^2 g^{-1}) of these hierarchitectures could improve the photocatalytic performance, as shown in Table 1. It has been reported that large surface area helps to increase the photocatalytic reaction sites and promote the efficiency of the electron-hole separation.[25] In addition, the porous nanoflowers with thinner laminar structures could not only benefit the transfer of the light-generated charge carriers to the surface to act with the organic molecules, but also allows the rapid diffusion of the reactants and products during the reaction.[26]

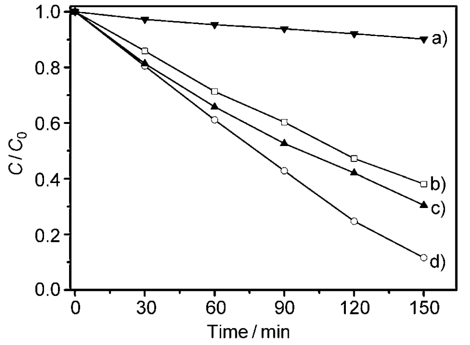

Figure 11. Photocatalytic degradation of RhB over a) commercial Bi_2O_3 product and the as-prepared samples obtained b) at 60 °C, $VO_3^- =$ 2 mmol L^{-1}; c) at 60 °C, $VO_3^- =$ 4 mmol L^{-1}; d) at 80 °C, $VO_3^- =$ 2 mmol L^{-1}, respectively.

Conclusion

In summary, we have developed a facile and template-free method for the controllable synthesis of Bi_2O_3 with unique flower-like hierarchitectures at 60–80 °C for 6 h. By properly monitoring the experimental conditions, such as the VO_3^- concentration, the reaction temperature, and the pH values, the Bi_2O_3 with different morphologies and microstructures could be obtained. On the basis of the observation of intermediate products in the growth process, a two-stage growth mechanism that involves an initial Ostwald ripening process followed by a self-assembly process is proposed. Moreover, the Bi_2O_3 hierarchitectures showed much higher (6–10 times) photocatalytic activity over commercial samples under visible light irradiation. The present work not only opens new strategies for the controllable synthesis of hierarchical nanostructures based on 2D nanoscale building blocks, but also provides a step forward in the design of photocatalysts with controllable morphology and enhanced photocatalytic activities.

Experimental Section

Synthesis: The Bi_2O_3 hierarchitectures were synthesized in an aqueous media in open system. In a typical experimental procedure, $Bi(NO_3)_3\cdot 5H_2O$ (0.5 mmol) and appropriate NH_4VO_3 were dissolved in 5 mL HNO_3 solution (4 $mol L^{-1}$). Then deionized water was added into this solution, which gave a final volume of 25 mL. After stirring for 10 minutes, NaOH was added to adjust the pH to 12. Yellow precipitates formed immediately. The suspension was heated at an appropriate temperature for 24 h without stirring. The final products were centrifuged, washed with deionized water and absolute ethanol for several times, and then dried at 60 °C for 10 h in air.

Characterization: The powder X-ray diffraction (XRD) patterns of the as-synthesized samples were measured on a D/MAX 2250 V diffractometer (Rigaku, Japan) using monochromatized CuK_α ($\lambda = 0.15418$ nm) radiation under 40 kV and 100 mA. The morphologies and microstructures of as-prepared samples were examined by using transmission electron microscopy (TEM, JEOL JEM-2100F; accelerating voltage: 200 kV) and scanning electron microscopy (SEM, JEOL JSM-6700F). High-resolution transmission electron microscopy (HRTEM) images were obtained by using JEM 2100F field-emission transmission electron microscope operated at an accelerating voltage of 200 kV. Nitrogen adsorption-desorption measurements were conducted at 77.35 K on a Micromeritics Tristar 3000 analyzer after the samples were degassed at 200 °C for 6 h. The Brunauer–Emmett–Teller (BET) surface area was estimated by using adsorption data in a relative pressure range from 0.05 to 0.3.

Photocatalytic tests: The photocatalytic activities of the Bi_2O_3 hierarchitectures were evaluated by the photocatalytic decolorization of a model pollutant Rhodamine-B (RhB) under visible light. A 500 W Xe lamp was used as a light source with a 420 nm cutoff filter to provide visible light irradiation. The experiments were performed at ambient temperature as follows: In each run, 50 mg of Bi_2O_3 catalyst was added into 50 mL RhB solution ($10^{-5} mol L^{-1}$). Before illumination, the suspension was stirred for 30 min in the dark to reach the adsorption-desorption equilibrium between the RhB and the photocatalyst. Then the suspension was stirred and exposed to visible light irradiation. The concentrations of the RhB were monitored by checking the absorbance at 553 nm during the photodegradation process by using a Hitachi U-3010 UV-vis spectrophotometer.

Acknowledgement

We acknowledge the financial support from the National Natural Science Foundation of China (No. 50672117, 50732004).

---

[1] a) M. Law, J. Goldberger, P. D. Yang, *Annu. Rev. Mater. Res.* **2004**, *34*, 83; b) J. T. Hupp, K. R. Poeppelmeier, *Science* **2005**, *309*, 2008; c) X. G. Peng, L. Manna, W. D. Yang, J. Wichham, E. Scher, A. Kadavanich, A. P. Alivisatos, *Nature* **2000**, *404*, 59; d) Z. L. Wang, J. H. Song, *Science* **2006**, *312*, 242; e) Y. N. Xia, P. D. Yang, Y. G. Sun, Y. Y. Wu, B. Mayers, B. Gates, Y. D. Yin, F. Kim, Y. Q. Yan, *Adv. Mater.* **2003**, *15*, 353; f) H. L. Xu, W. Z. Wang, *Angew. Chem.* **2007**, *119*, 1511; *Angew. Chem. Int. Ed.* **2007**, *46*, 1489.

[2] a) W. N. Li, J. Yuan, X. F. Shen, S. Gomez-Mower, L. P. Xu, S. Sithambaram, M. Aindow, S. L. Suib, *Adv. Funct. Mater.* **2006**, *16*, 1247; b) C. Z. Wu, L. Y. Lei, X. Zhu, J. L Yang, Y. Xie, *Small* **2007**, *3*, 1518; c) X. M. Ni, Q. B. Zhao, D. G. Zhang, X. J. Zhang, H. G. Zheng, *J. Phys. Chem. C* **2007**, *111*, 601; d) Y. Y. Li, J. P. Liu, X. Huang, G. Li, *Cryst. Growth Des.* **2007**, *7*, 1350.

[3] a) B. X. Li, Y. Xie, Y. Xue, *J. Phys. Chem. C* **2007**, *111*, 12181; b) M. H. Cao, X. Y. He, J. Chen, C. W. Hu, *Cryst. Growth Des.* **2007**, *7*, 170.

[4] Z. N. Adamian, H. V. Abovian, V. M. Aroutiounian, *Sens. Actuators B* **1996**, *35–36*, 241.

[5] L. Leontie, M. Caraman, M. Delibas, G. I. Rusu, *Mater. Res. Bull.* **2001**, *36*, 1629.

[6] B. Yang, M. Mo, H. Hu, C. Li, X. Yang, Q. Li, Y. Qian, *Eur. J. Inorg. Chem.* **2004**, 1785.

[7] L. Leontie, M. Caraman, M. Alexe, C. Harnagea, *Surf. Sci.* **2002**, *507*, 480.

[8] V. Fruth, M. Popa, D. Berger, R. Ramer, M. Gartner, A. Ciulei, M. Zaharescu, *J. Eur. Ceram. Soc.* **2005**, *25*, 2171.

[9] H. T. Fan, X. M. Teng, S. S. Pan, C. Ye, G. H. Li, L. D. Zhang, *Appl. Phys. Lett.* **2005**, *87*, 231916.

[10] Y. F. Qiu, D. F. Liu, J. H. Yang, S. H. Yang, *Adv. Mater.* **2006**, *18*, 2604.

[11] T. Takeyama, N. Takahashi, T. Nakamura, S. Itoh, *Solid State Commun.* **2005**, *133*, 771.

[12] J. C. Yu, A. W. Xu, L. Z. Zhang, R. Q. Song, L. Wu, *J. Phys. Chem. B* **2004**, *108*, 64.

[13] a) L. Li, Y. W. Yang, G. H. Li, L. D. Zhang, *Small* **2006**, *2*, 548.

[14] a) N. M. Sammes, G. A. Tompsett, H. Näfe, F. Aldinger, *J. Eur. Ceram. Soc.* **1999**, *19*, 1801; b) W. Zhou, *J. Solid State Chem.* **1990**, *87*, 44; c) P. Shuk, H. D. Wiemhöfer, U. Guth, W. Göpel, M. Greenblatt, *Solid State Ionics* **1996**, *89*, 179; d) L. Leontie, M. Caraman, A. Visinoiu, G. I. Rusu, *Thin Solid Films* **2005**, *473*, 230.

[15] R. Punn, A. M. Feteira, D. C. Sinclair, C. Greaves, *J. Am. Chem. Soc.* **2006**, *128*, 15386.

[16] J. W. Mullin, *Crystallization*, 3rd ed., Butterworth-Heinemann, London, **1997**, p 288.

[17] a) J. A. Nucci, R. D. Keller, P. Field, Y. Shacham-Diamand, *Appl. Phys. Lett.* **1997**, *70*, 1242; b) G. Xi, K. Xiong, Q. Zhao, R. Zhang, H. Zhang, Y. Qian, *Cryst. Growth Des.* **2006**, *6*, 577.

[18] a) A. Kudo, K. Omori, H. Kato, *J. Am. Chem. Soc.* **1999**, *121*, 11459; b) Y. Yu, C. Jin, R. Wang, Q. Chen, L. Peng, *J. Phys. Chem. B* **2005**, *109*, 18772.

[19] a) L. Zhou, W. Wang, L. Zhang, H. Xu, W. Zhu, *J. Phys. Chem. C* **2007**, *111*, 13659; b) L. Zhou, W. Wang, H. Xu, *Cryst. Growth Des.* **2008**, *8*, 728.

[20] a) D. V. Bavykin, V. N. Parmon, A. A. Lapkin, F. C. Walsh, *J. Mater. Chem.* **2004**, *14*, 3370; b) J. Yu, H. Yu, B. Cheng, C. Traplis, *J. Mol. Catal. A* **2006**, *249*, 135.

[21] Y. Li, J. Liu, X. Huang, G. Li, *Cryst. Growth Des.* **2007**, *7*, 1350.

[22] C. Zhang, Y. Zhu, *Chem. Mater.* **2005**, *17*, 3537.

[23] M. A. Butler, *J. Appl. Phys.* **1977**, *48*, 1914.

[24] a) V. Dolocan, *Appl. Phys.* **1978**, *16*, 405; b) L. Leontie, M. Caraman, M. Alexe, C. Harnagea, *Surf. Sci.* **2002**, *507*, 480.

[25] a) J. Tang, Z. Zou, J. Ye, *Chem. Mater.* **2004**, *16*, 1644; b) J. G. Yu, J. F. Xiong, B. Cheng, S. W. Liu, *Appl. Catal. B* **2005**, *60*, 211; c) L. Zhang, W. Wang, L. Zhou, H. Xu, *Small* **2007**, *3*, 1618;

[26] a) X. Wang, J. C. Yu, C. Ho, Y. Hou, X. Fu, *Langmuir* **2005**, *21*, 2552; b) L. Zhang, J. C. Yu, *Chem. Commun.* **2003**, 2078; c) Z. Y. Liu, D. D. Sun, P. Guo, J. O. Leckie, *Chem. Eur. J.* **2007**, *13*, 1851.

Received: June 23, 2008
Revised: September 28, 2008